

# Monadic Pavlovian associative learning in a backpropagation-free photonic network

James Y. S. Tan<sup>1†</sup>, Zengguang Cheng<sup>1,2†</sup>, Xuan Li<sup>1</sup>, Nathan Youngblood<sup>1,3</sup>, Utku E. Ali<sup>1</sup>, C. David Wright<sup>4</sup>, Wolfram H. P. Pernice<sup>5,6</sup> and Harish Bhaskaran<sup>1\*</sup>

<sup>1</sup>Department of Materials, University of Oxford, Parks Road, Oxford OX1 3PH, UK.

<sup>2</sup>Current address: State Key Laboratory of ASIC and System, School of Microelectronics, Fudan University, Shanghai 200433, China.

<sup>3</sup>Current address: Department of Electrical and Computer Engineering, University of Pittsburgh, 3700 O'Hara St., Pittsburgh, PA 15261, USA

<sup>4</sup>Department of Engineering, University of Exeter, Exeter EX4 4QF, UK.

<sup>5</sup>Institute of Physics, University of Muenster, Heisenbergstrasse 11, 48149 Muenster, Germany.

<sup>6</sup>Center for Soft Nanoscience, University of Muenster, 48149 Muenster, Germany

<sup>†</sup>These authors contributed equally to this work.

\*Corresponding author. Email: harish.bhaskaran@materials.ox.ac.uk

## Abstract

Over a century ago, Ivan P. Pavlov, in a classic experiment, demonstrated how dogs can learn to associate a ringing bell with food, thereby causing a ring to result in salivation. Today, however, it is rare to find the use of Pavlovian type associative learning for artificial intelligence (AI) applications. Instead, other biologically-inspired learning concepts, in particular artificial neural networks (ANNs) have flourished, yielding extensive impact on a wide range of fields including finance, healthcare and transportation. However, learning in such ‘conventional’ ANNs, in particular in the form of modern deep neural networks (DNNs) are usually carried out using the backpropagation method, is computationally and energy intensive. Here we report the experimental demonstration of backpropagation-free learning, achieved using a single (or monadic) associative hardware element. This is realized on an integrated photonic platform using phase change materials combined with on-chip cascaded directional couplers. We link associative learning with supervised learning, based on their

common goal of associating certain inputs with ‘correct’ outputs. We then expand the concept to develop larger-scale supervised learning networks using our monadic Pavlovian photonic hardware, developing a distinct machine-learning framework based on single-element associations and, importantly, using backpropagation-free single-layer weight architectures to approach general learning tasks. Our approach not only significantly reduces the computational burden imposed by learning in conventional neural network approaches, thereby increasing speed and decreasing energy use during learning, but also offers higher bandwidth inherent to a photonic implementation, paving the way for future deployment of fast photonic artificially intelligent machines.

## Introduction

The constant interaction of living beings with one another as well as their environment has long been recognized as important in their cognitive development (1,2). Psychological adaptations to changing conditions allow them to evolve continuously to fit themselves into the immediate local surrounding. Inspired by their ability to integrate sensing, reasoning and thinking via adaptations to dynamically changing circumstances, AI seeks to build, engineer, control and design neuromorphic networks that are on par with, or perhaps even more elegant than, biological neural networks (3-5).

In nature, the ability to associate sensory cues is often linked to the ability of living beings to solve complex multivariate problems with relative ease. Inspired by the same principles, such associative learning has been used to augment human capabilities, for example, to provide the ability to predict rare events from temporal and sequential patterns of timestamped observations (6,7). The ability to decipher non-trivial patterns in data using computational techniques has facilitated sophisticated machine intelligence with a plethora of data analytic applications (8-11). Such computations, however, have predominantly been performed on general-purpose digital electronic processors (i.e. GPUs and CPUs). Special-purpose hardware accelerators designed to implement such computing tasks are needed to decrease computational latency and increase data throughput (12-16). Additionally, harnessing the inherent property of photonics to carry out parallel operations simultaneously via wavelength-multiplexing will greatly increase the capacity of intelligent information processing. Practical associative learning hardware accelerators require a hardware device structure that can associate inputs on a device. Thus far, associative learning devices that have been developed on electronic (17-27), optoelectronic (28), and synthetic biological (29) platforms rely on multiple elements (for example, arithmetic and/or Boolean logic gate circuit components) (17-27), or large area thin film structures that depend on free space data inputs

(28). The ability to monadically associate at least two inputs together is distinctly absent at a device level; however monadic associations can enable device simplicity for straightforward backpropagation-free single-layer weight neural network architectures that facilitate quicker training convergence rate, as we will show. In this paper, we address this need for single associate learning elements that can deliver high bandwidth and has the potential for a future scalable artificial neural network (6,7,30).

### **Associative Monadic Learning Element (AMLE) concept**

In biological systems, a fundamental associative learning process – classical conditioning - can be described as the neural circuit in Fig. 1a (31,32). The unconditioned stimulus (*UCS*) is the input from a sensory neuron (blue) that naturally triggers the response from a motor neuron (green), while the neutral stimulus (*NS*) is the input from another sensory neuron (red) that does not normally trigger the response until it is ‘associated’ (or ‘temporally paired’) with the *UCS*. After the association is established, the response is triggered when either the *UCS* or the conditioned stimulus (*CS*, previously *NS*) is sent to the motor neuron. Classical conditioning was initially ascertained by ‘Pavlov’s dog experiment’ in 1901 (33). In the experiment, food was the *UCS* that triggered an unconditioned response (*UCR*) i.e., the dog’s salivation; while the ringing bell sound was the *NS* or *CS*. The bell (*NS/CS*) only triggered the salivation response after the ringing bell was associated by the dog with the repletion of food. Two main roles of this simplified neural circuitry can be identified: one, to converge and associate the two inputs, namely the *UCS* and *NS/CS* sensory inputs; and secondly, to store memories of these associations *in situ*.

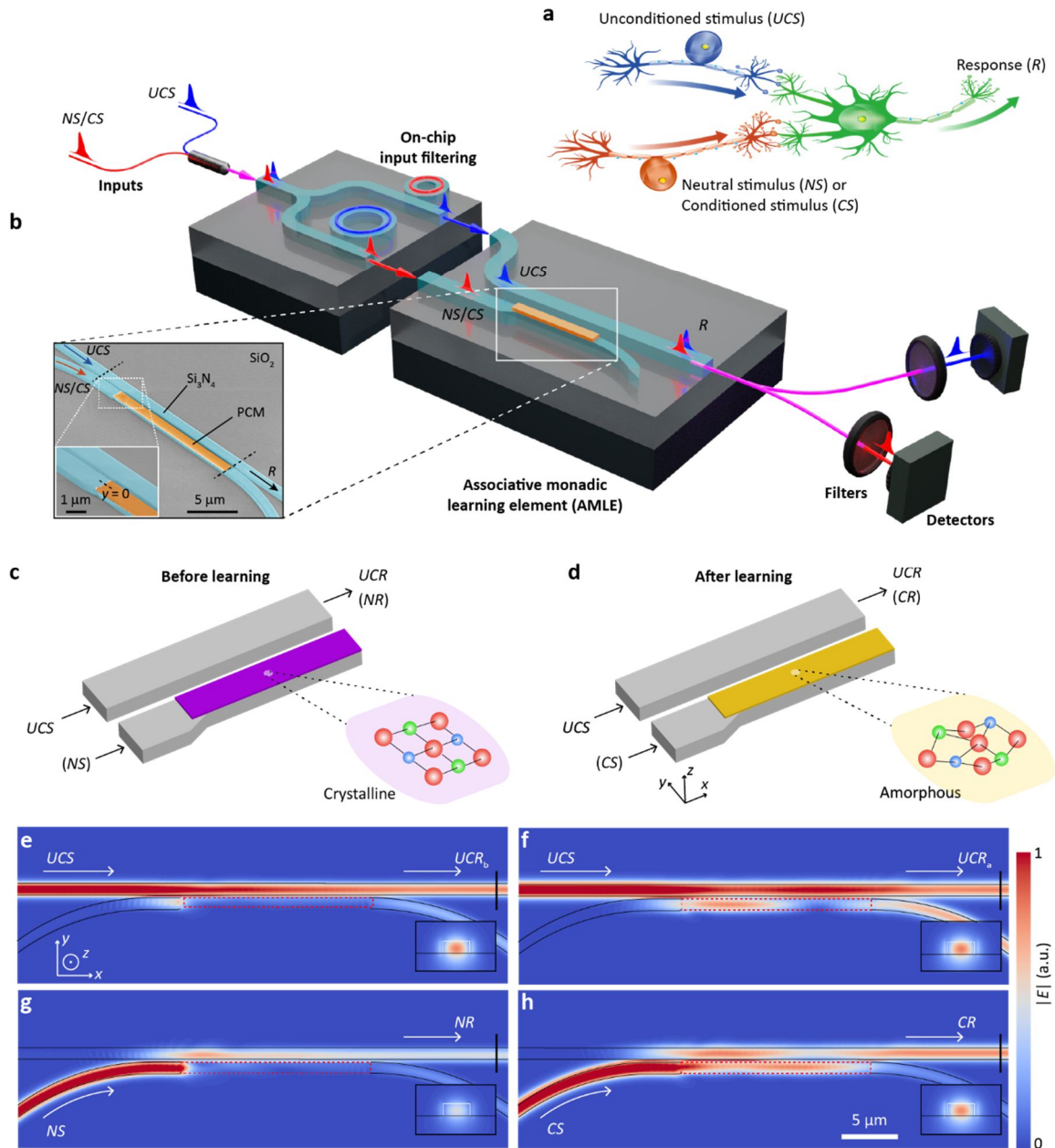


**Fig. 1. An optical associative monadic learning element (AMLE).**

**a.** Simplified illustration of the neural circuitry for associative learning. After *NS* is persistently paired with *UCS*, it is conditioned (*CS* in order to distinguish it from the unconditioned *NS*) to the same response as the *UCS*. **b.** Schematic drawing of an on-chip measurement layout of the optical AMLE (boxed). Two laser sources that represent the *UCS* and *NS/CS* stimulus are combined into the on-chip layout which splits to two waveguide paths. The input signal components in these paths are then selectively filtered by the waveguide-ring resonators such that the inputs to AMLE is only of *UCS* or *NS/CS* signals. The resulting output responses of AMLE are filtered and detected. Inset: SEM image (false colored) of a fabricated AMLE, consisting of two cascaded  $\text{Si}_3\text{N}_4$  directional couplers (cyan),  $\text{SiO}_2$  undercladding (grey) and PCM cell (marigold). **c-d.** The effect of association, which results in PCM structural phase change on AMLE, is manifested by its overall output response. Before learning

(crystalline PCM) in **c**, after learning (amorphous PCM) in **d**. This relation is a signature of associative learning  $NS/CS \rightarrow UCS$ . **e-h**. Corresponding electric field profile of AMLE before (**e** and **g**) and after (**f** and **h**) learning, with  $UCS$  (**e** and **f**) and  $NS/CS$  (**g** and **h**) inputs respectively. Inset: Output cross-section electric field profiles at locations denoted by black vertical bars. The color bar is normalized.

In our optical design, we embedded these two complementary roles (association and memory) in the form of a novel associative learning element, which consists of two coupled waveguides (Fig. 1b inset). Initially, the optical power ( $UCS$  and  $NS/CS$ ) is entirely guided in the lower waveguide which switches a fractional volume of a phase-change material (PCM) cell integrated on (deposited on top of) the bottom waveguide into a new state (more amorphous). With more converging learning pulses, a larger volume of material switches from the crystalline to the amorphous state, until reaching a learning threshold. This process is akin to that used in non-volatile PCM photonic memories (34), but in this case, we employ the optical phase difference between  $NS/CS$  and  $UCS$  inputs to precisely control the solid state of the material. This enables us to establish the extent of association between the inputs. The PCM deposited on the lower waveguide is the well-known germanium antimony tellurium alloy  $Ge_2Sb_2Te_5$  (GST), with ultrafast structural phase transition time (sub-ns amorphization and few-ns crystallization time (35)), high cycling endurance ( $\sim 10^{12}$  cycles (36,37)), and long retention time ( $>10$  years at room temperature (37)). A thin capping layer of indium tin oxide (ITO) was additionally deposited on the phase change material to prevent oxidation, and to help localize optically-induced heat to enable low-power PCM structural phase switching (34,38).

Analogous to the biological neural mechanism of associative learning (31,32), the association between  $UCS$  and  $NS/CS$  during the learning process occurs only when the two inputs are paired at a specific time delay  $\Delta t$ , resulting in a change in synaptic weight  $\Delta w$  between the  $UCS$  and  $NS/CS$  inputs and output  $R$ . In our AMLE, the time delay  $\Delta t$  is

represented by the relative time delay introduced by the optical phase difference between the *UCS* and *NS/CS* inputs, i.e.  $\Delta t = t_{UCS} - t_{NS/CS}$ , where  $t_{UCS}$  and  $t_{NS/CS}$  are the times at which the respective optical field input signals *UCS* and *NS/CS* are referenced to the same optical phase. Under normal circumstances, the slightest vibration and/or temperature change in the measurement environment can cause the optical phases to vary erratically. We address this challenge of phase delay control and stability by designing an on-chip layout integrated onto the AMLE, as depicted in in Fig. 1b. Such disturbance is absent on-chip due to the mechanically rigid substrate that acts as a natural heat sink. The layout locks the time delay of the phases (phase delay) as a function of spatial path length difference from an optical splitter to the input ports of the AMLE. To control the input signal combinations (*UCS* only, *NS/CS* only, and both *UCS* and *NS/CS*) that make up the two inputs, we couple wavelength-selective critically-coupled ring resonators to each of the inputs leading to the AMLE. This enables us to choose either the *UCS* or the *NS/CS* inputs to be active when the input to the on-chip layout is at the resonant wavelength of the bottom or top ring resonator, respectively. The optical wavelength of the input laser source routes both the single- and two- input incidences to the AMLE. While Fig. 1b highlights the use of ring resonators to activate the inputs to the AMLE by depicting using only two input signals, the layout requires using signals of three different optical wavelengths – one for the learning process (enabled by using optical wavelength that is neither of the ring resonance wavelengths), and two others to probe the process in real-time via *UCS*-only and *NS/CS*-only inputs. Simultaneous real-time monitoring of the AMLE is carried out by using an optical combiner which joins the *UCS* and *NS/CS* inputs from the laser sources and photodetector to measure the output transmission.

We use coupled mode theory (39) to design the AMLE to determine the input combinations that trigger the associative learning process, and for regulating the output response  $R$ . The structural phase difference (crystalline and amorphous) of the PCM translates

to optical loss contrast, which we exploit to define the output responses of the AMLE before and after learning. For the pump/learning inputs, we designed the device such that both the inputs to the AMLE has to be of the same optical wavelengths at a fixed  $\Delta t$ . This enables optical field from both the inputs to accumulate and sufficiently switch the PCM on the AMLE during the learning process. The use of directional couplers ensures that the design is applicable over a broad optical wavelength range.

The operational principle of probing the AMLE is illustrated in Fig. 1c and d. Based on the optimized geometry, we verified our theoretical calculations using three-dimensional finite difference time domain FDTD numerical simulations of the AMLE before and after learning (crystalline and amorphous PCM) upon excitation by a transverse electric TE optical field input at 1580 nm wavelength. As summarized in the figures, before learning, input *UCS* naturally triggers output *UCR*, while input *NS* does not trigger a *UCR*-like output (denoted here as the neutral response *NR*) until paired with *UCS*. After learning, input *CS* (which was input *NS* before learning) now triggers *CR* – a response similar to *UCR*. Fig. 1e-h shows input *NS/CS*  $\rightarrow$  input *UCS* association in our simulations, with the before learning case in Fig. 1e and 1g, and the after learning case in Fig. 1f and 1h. The corresponding output cross-sectional field profile before and after learning upon *UCS* and *NS/CS* input incidence are shown in the insets of Fig. 1e-h. The clear contrast between *NR* and *CR/UCR* outputs confirms the input *NS/CS*  $\rightarrow$  input *UCS* association after learning.

### **Observation of photonic associative learning**

We now experimentally characterize the dynamic response of the AMLE. The associative process relies on the optical phase difference between the inputs, which requires stable control of optical phases in our measurements. To completely rid the effects of off-chip disturbances to the stability of optical phases, we run our experiments on the on-chip layout



represented in Fig. 1b, using different wavelengths for the pump and probes to measure the output response from different inputs in real-time. This allows us to understand the dynamics of the associative learning process by avoiding any unwanted pump-probe optical interference.

The starting point of the AMLE is its fully crystalline state (we achieve this by annealing the chips on a hotplate at  $\sim 250^\circ\text{C}$  for 10 min to completely crystallize the PCM, and then stabilize the PCM states; see Methods). While sending the *UCS* and/or *NS/CS* input pump pulses to the AMLE, we probe the output transmission readouts in real-time using different wavelengths. The results are shown in Fig. 2a. As plotted at the bottom graph of the figure in events 1-4, the transmission readouts remained the same for single input pulse incidence. When we sent both *UCS* and *NS* pump pulses together with a fixed phase delay at 13.2 mW each in event 5, the transmission change ( $\Delta Tr / Tr_0$ ) for the *UCS* and *NS* probe readouts changed by  $\sim -4\%$  and  $\sim +4\%$  respectively. As the input pump pulse power was ramped up from 6.6 mW to 14.5 mW in events 6-8, the probe readouts further changed by nearly  $-7\%$  and  $+7\%$  respectively, both of which were well above the *UCR/CR* response threshold at  $Tr \sim 0.07$ .

The reversibility of the associative learning process is further shown in Fig. 2b. A set of pulses at 4.3 mW in event 9, followed by 1.9 mW pulses in event 10 resulted in the ‘forgetting’ process, where the readouts  $Tr$  reverted to the baselines ( $Tr_0 \sim 0.14$  for *UCS* input probe and  $Tr_0 \sim 0$  for *NS/CS* input probe). For our measurements, readout above  $Tr \sim 0.05$  is designated for the presence of output response *UCR/CR* (salivation present). As simplified in the illustration of Fig 2a (inset), the associative learning process is realized entirely on the monadic element, within which the *UCS* connection synaptic weight  $w_1$  and *NS/CS* connection synaptic weight  $w_2$  are simultaneously yet independently modified only when the two inputs arrive together depending on  $\Delta t$ .

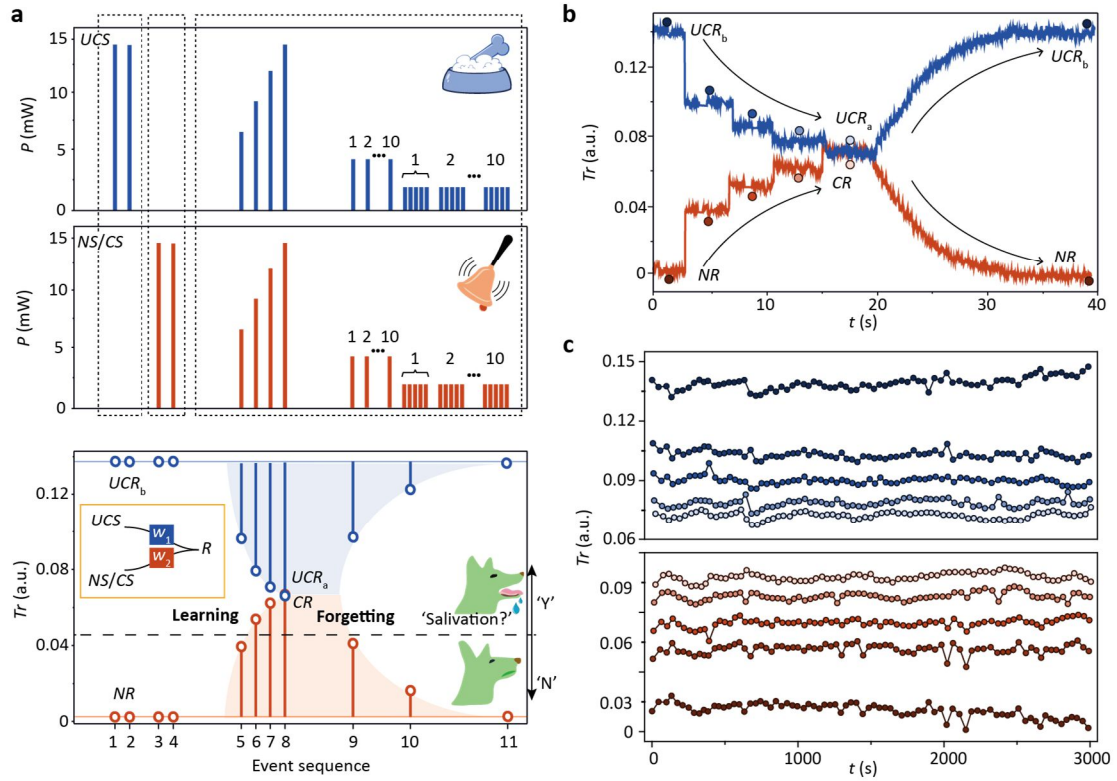


**Figure 2. Photonic Pavlovian learning process.**

**a.** Input-output relation of AMLE  $UCS$  and  $NS/CS$  inputs (blue and red charts) denote ‘Food’ and ‘Bell’ inputs; the corresponding output transmission  $Tr$  (bottom plot) represents the response. Bottom chart inset: Simplified diagram of AMLE. **b.** Corresponding real time probe transmission  $Tr$  of the learning and forgetting processes in **a.** **c.** Repeatability of the processes on AMLE over 80 cycles. Different curves corresponding to the levels denoted by the disks with the same colors in **b.**

Fig. 2b shows a single cycle of the real time  $UCR/CR$  output readout of associative learning in events 5-8, and forgetting process in events 9-10 of Fig. 2a. To test the long-term durability, we subjected the AMLE through 80 learning cycles, examined over a period of 40 minutes. Even after the 80 cycles (Fig. 2c), the individual learning weights were clearly identifiable with deviation of each weights below 0.69% in readout transmission.

### Associative learning for supervised learning

Up to this point, we have observed associative learning and characterized the inner workings in our optical measurements. The general concepts of Pavlovian associative learning

(Fig. 3a) and supervised learning (a class of machine learning; Fig. 3b) are in essence comparable – both involving the pairing of input ( $IN$ ) with the correct output ( $Teacher$ ) to supervise the learning process. However, the exact network constituents that map the input to the output in conventional supervised learning architectures are fundamentally distinct – the  $Teacher$  signal propagates backward layer-by-layer to collectively adjust the network weights such that the actual output  $R$  better resembles the desired output ( $Teacher$ ) after each learning iteration. To reinforce the relation between associative learning with supervised learning, we provide in Fig. 3c a solution to the problem, which we implement on an optical chip.

While the previous layout (Fig. 1b) allows us to observe associative learning in real-time, the layout in Fig. 3c (adapted from that in Fig. 1b) enables the integration of multiple AMLEs on a single platform using wavelength-multiplexed inputs. One of the key hallmarks of photonic signal transmission and processing is the increased capacity for a multitude of data on a single channel via wavelength multiplexing that enables larger amounts of data to be transmitted simultaneously. Here, we wavelength-multiplex the input combination signals in the network at the input layer, which consists of the inputs mapped to the possible input combinations, before these combinations are paired with the  $Teacher$  input at the associative layer to cumulatively produce an output response  $R$  (30). The network architecture in Fig. 3c for the example when the input  $(IN_1, IN_2) = (0,1)$  is sent (with  $Teacher = 1$ ) is summarized in Fig. 3d. We represent in the network schematics the input mappings using two kinds of arrows i.e., pointed and circle arrows that respectively direct and negate the signals directly to the nodes. The succeeding nodes (including that of the AMLEs in bordered boxes) are activated when all converging arrows carry a signal.

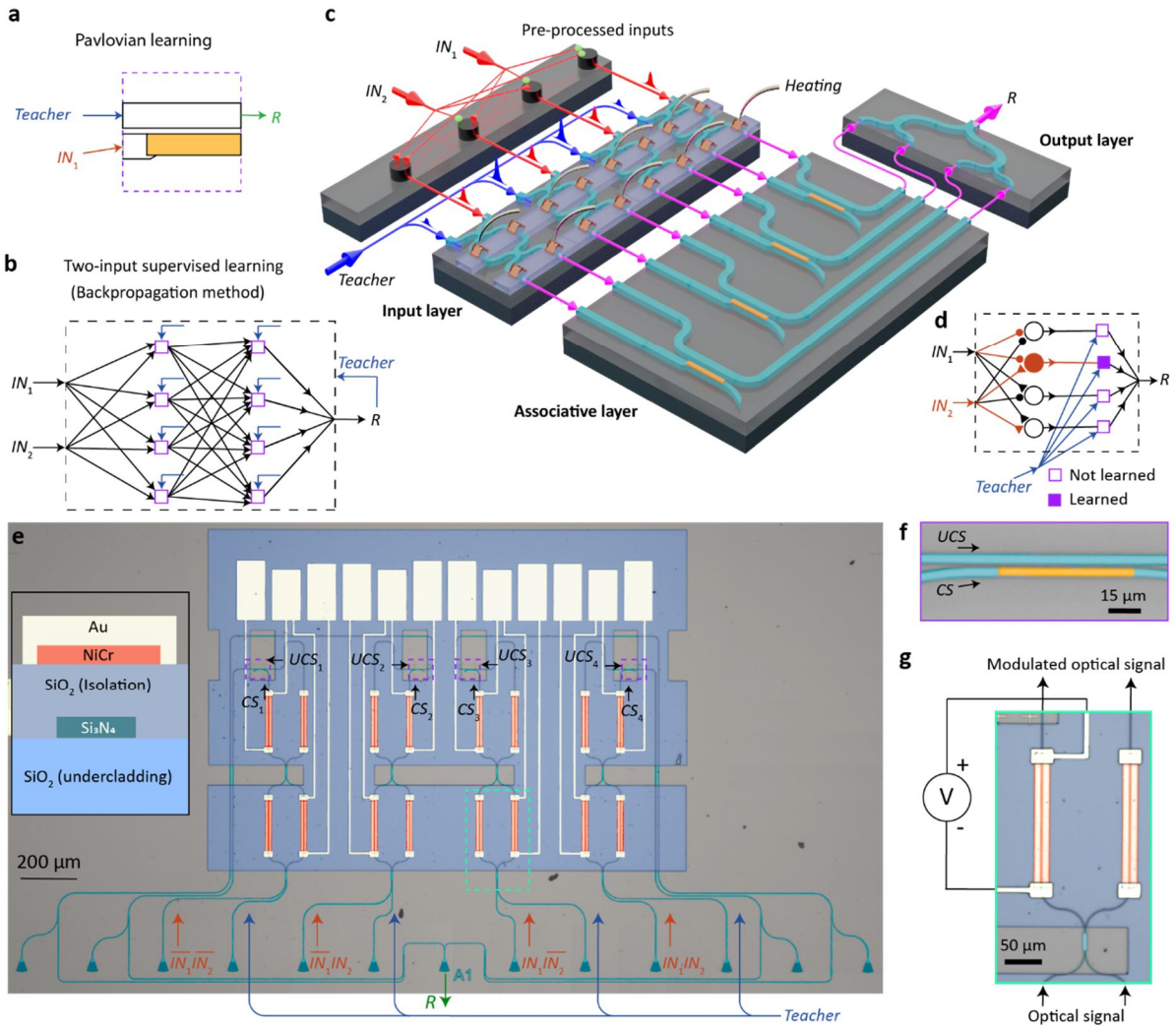


**Figure 3. Supervised Pavlovian associative learning.**

**a.** Pavlovian learning involves pairing the inputs ( $IN$ ) with the correct outputs ( $Teacher$ ) to supervise the learning process. **b.** Current conventional supervised learning networks use backpropagation. The network diagram depicts the network for a two-input supervised learning. **c.** Optical on-chip hardware diagram of supervised learning with two inputs using AMLE. The input signals  $IN_1$  and  $IN_2$  fed into the system during the learning process are translated to their four possible combinations to be supervised by the  $Teacher$  input signal. The combination of the inputs signals from the  $IN_1$ ,  $IN_2$  and  $Teacher$  inputs leading to the AMLE are controlled by thermo-optic NiCr heaters. **d.** Network representation of the hardware diagram in **c**. **e.** Optical micrograph of supervised learning network in **c**, which consists of four AMLEs (boxed, purple). The arrows show the optical input-output connections coupled to the on-chip network via grating couplers. **f, g.** Optical micrographs of a single AMLE and a heater respectively correspond to those in **d**.

We translate the network model (schematic network drawn in Fig. 3c, and in Fig. 3d) to an integrated chip shown in Fig. 3e. The network consists of the associative layer (purple bordered boxes) between an input layer (input data and input *Teacher* label, denoted using red and blue arrows respectively) and an output layer (response  $R$ ; green arrow). The NiCr thermo-optic heaters (green bordered boxes) enable the control of optical signal paths between the input layer and the associative layer. Optical micrographs with an enlarged view of the AMLE and thermo-optic heaters are shown in Figure 3f and 3g respectively, with the depiction of AMLE consistent with prior descriptions in Fig. 1b. The thermo-optic heaters, which control the optical phases and thus connections between the input layer to the associative layer, are modulated using external voltage sources via on-chip gold electrodes.

The modulation of inputs to the AMLEs in Fig. 3e is based on the measurement scheme shown in Fig. 4a. The input incidences are precisely configured using on-chip heaters. These heaters, placed on the arms of the two interferometers, can be thought of as an abstraction layer that defines the amplitudes and phases of the inputs to the element. Given that the optical wavelength of the two inputs to AMLE has to be equal for the pump/learning process, this layer is essential to enabling wavelength-multiplexed inputs on our large-scale platform because it provides a reliable means to split the *Input* and *Teacher* signals equally with stable optical phases to the AMLEs (see Fig. 4a). When the  $(IN_1, IN_2)$  input combinations and the *Teacher* to the AMLE are both activated during training, the individual  $AMLE_i$  yields the output response  $R_i = 1$  (salivation), where  $i$  ranges from  $i = 1$  to  $i = 2^M$  ( $M$  is the input dimensions). The net output response of the  $AMLE_i$  is the summation of the output responses  $R_i$ . Before the experiment, the PCM cells were set to their crystalline state (see Methods). In line with the Boolean eXclusive OR (XOR) logic gate input-output relations, the four possible  $(IN_1, IN_2)$  input combinations:  $(IN_1, IN_2) = (0,0), (0,1), (1,0)$  and  $(1,1)$  correspond to the *Teacher* input 0,1,1,0. We translate the 0 and 1 logic input values to corresponding pump input (of 0 and 14.7

mW respectively in this case) and use this input pump scheme to deliver the  $(IN_1, IN_2)$  pump input combination pulses with its corresponding *Teacher* pump input pulses during training.

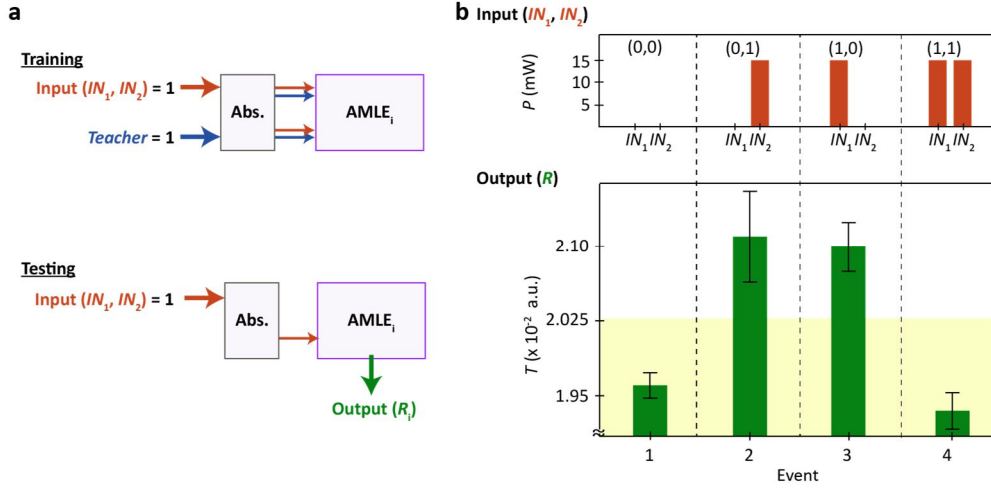


**Figure 4. Experimental demonstration of Pavlovian supervised learning.**

**a.** When both the input combinations  $(IN_1, IN_2)$  and *Teacher* are activated during training, the input combinations  $(IN_1, IN_2)$  signal produces the individual output response  $R_i = 1$ . The net output response  $R$  is the summation of the individual output responses  $R_i$ . The abstraction layer (labelled ‘Abs.’) between  $(IN_1, IN_2)$ , *Teacher* signals and  $AMLE_i$  sets and controls the amplitude and phases to the  $AMLE_i$ . In our case, this layer is the thermo-optic heaters on the interferometers. **b.** Experimental demonstration of supervised learning on the network in Fig. 3e. The  $IN_1$  and  $IN_2$  inputs (top chart) denote the inputs to the network, while the corresponding net output response transmission readouts  $T$  (bottom plot) represent the net output of the associative learning network. After the temporal pairings of  $(IN_1, IN_2)$  and *Teacher* input pump pulses, the network learns to associate with the set of values from the *Teacher* input 0,1,1,0 for the  $(IN_1, IN_2)$  input combinations (0,0), (0,1), (1,0) and (1,1), where the top of the yellow box represents the threshold chosen.

After each training event, we probe the output transmission  $T$  by feeding the corresponding  $(IN_1, IN_2)$  probe inputs. The experiment is repeated for 6 trials, with the transmission mean and standard deviation represented in Figure 4b. The threshold value was assigned at  $T = 2.025 \times 10^{-2}$  such that transmission above and below the threshold represents the values 1 and 0, respectively. As shown, the associative network successfully classifies the pattern 0,1,1,0 after the learning trials: the output transmission is above the threshold only when the input probe  $(IN_1, IN_2)$  is (0, 1) or (1,0). We note that crucially, the associative network

contains only single layer weights (on the AMLE) to solve the XOR nonlinear classification problem. Such a straightforward approach to supervised learning guarantees faster learning convergence compared to other conventional approaches (40,41). For example, conventional approaches using gradient descent or metaheuristic genetic algorithms require incremental steps to convergence minima and exhaustive search for solutions to the learning problem.

The pattern recognition task described above is specialized to recognizing a specific pattern, from which the input set corresponds specifically to an XOR output set. In many practical applications, it is important to create a good predictive model that is capable of generalizing a set of patterns, instead of recognizing one particular pattern. Here, we demonstrate how AMLE-based hardware can achieve generalization on an image recognition task using associative learning, based on the network architecture shown in Fig. 5a. The network is similar to those in Fig. 3d, which consists of three main network layers (i.e., input layer, associative layer and output layer) (30).

During the training process, images to be trained are first pixelated to  $15 \times 13$  input pixel data. These data, which we represent in the form of eight possible *Input* combinations  $IN_1$ - $IN_8$ , are then sent to the resulting associative layer. The *Teacher* signals, which dictate the image to be recognized, are likewise preprocessed and sent to the associative layer at the same time as the *Input* signals. This induces a change in the state of the AMLEs upon spatiotemporal co-occurrences between the thresholded *Input* and *Teacher* signals. The change in the learning states of AMLEs is determined from its transmission readouts, when a preprocessed *Input* data of maximum amplitude and same dimensions (blank white image) is fed through the layers. The transmission of these individual  $AMLE_i$  are summed up at the output layer and rearranged to form a  $15 \times 13$ -pixel model representation. The complete net representation is obtained by cumulatively adding the model representation from each training pair. Pixel-by-pixel



comparison between the net model representation (which generalizes the training images) and testing images is then made to determine if the testing images are of the image to be detected.

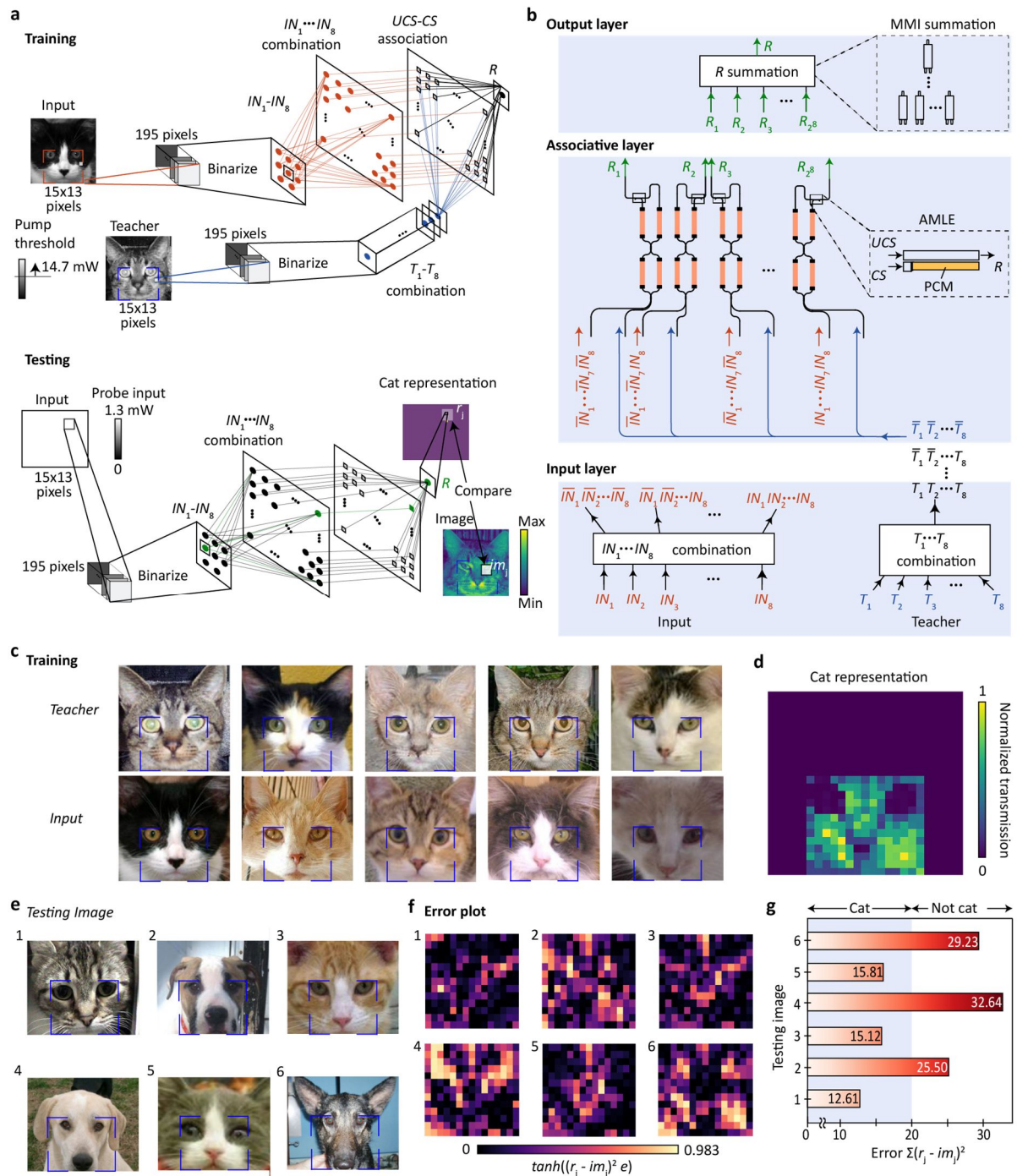


**Figure 5. Scaling architecture for image recognition using associative learning network.**

**a.** The general associative neural network composed of an input layer ( $IN_1$ - $IN_8$ ,  $T_1$ - $T_8$ ), associative layer (UCS-CS association) and output layer ( $R$ ). The input signal is the pattern (pixels from image) to be



classified, and the external teacher provides the desired set of output values chosen to represent the class of patterns being learned. During training, the input layer converts the input signal ( $IN_1-IN_8$ ) and external teacher ( $T_1-T_8$ ) signal from the images to a combination of data ( $IN_1-IN_8$  combinations,  $T_1-T_8$  combinations) before being fed into the associative layer. The associative layer consists of AMLEs with states that are modified when both the input and external teacher signals are paired together. A model representation of the trained images are then obtained by sending a preprocessed input signal of blank white image to propagate through the layers. **b.** Optical on-chip implementation of the input layer, associative layer and output layer respectively. The associative layer, which consists of thermo-optic NiCr heaters, distributes the combination of the input and external teacher signals (from the input layer) as *UCS* and *CS* inputs to the respective AMLEs. The output layer consists of a summation unit to sum up the output response from the AMLEs to form the net output. **c.** Training the associative learning network to identify cat images, with bounding box corners to indicate region of interest. **d.** After five training iterations, the network learns the model representation of cat from the output response  $R$ . **e.** Images used to test if the network can correctly classify pictures as cat and non-cat. **f.** Error plot to visualize the pixel-to-pixel  $j$  difference between the testing image  $im$  with the model representation  $r$  in **d.** **g.** The network successfully recognized cat and non-cat images based on the squared Euclidean distance  $\Sigma (r_j - im_j)^2$  measured over the testing images for each of the  $15 \times 13$  pixels.

The photonic implementation of the associative learning network architecture is shown in Fig. 5b. Here, the PCM weights on the AMLEs are first initialized the crystalline state before the signals are sent to the on-chip photonic structure. During training, depending on the optical signal input combinations and the input pump power sent to the AMLEs, the state of the PCMs on AMLEs either remain in crystalline, or structurally switch to amorphous state. This results in a change in optical probe output response of the AMLEs. The individual responses  $R_i$  of  $AMLE_i$ , taken together using multimode interferometers (MMI), gives the net response  $R$ . In our experiment, we account for all the AMLEs in the image recognition network using the  $N = 4$  hardware AMLEs (see Fig. 3e) by assigning the update  $i \bmod (N) \rightarrow i$  to each  $AMLE_i$  in the image recognition network.

We examine the cat image classification capabilities of the associative learning network using the ‘Dogs vs Cats’ dataset from fast.ai (42) (single dataset collected from CIFAR10,

CIFAR 100 (43), Caltech 101 (44), Oxford-IIIT Pet (45) and Imagewoof (46)). The cat images that we used for the training process are shown in Fig. 5c. We note that in the training *Input* images, we included images of cats that have features that are less common (e.g., of a less common breed in *Input 4*, and of a kitten in *Input 5*). The *Teacher* images, on the other hand, contain images of cats that have common cat features and are easily recognizable cats. After the training process using the images in Fig. 5c, we obtain the model representation of a cat shown in Fig. 5d by feeding in a 15×13 pixel test input of maximum probe input power magnitude (1.3 mW).

Thus far, we demonstrated searching for patterns (in the form of pixel amplitudes) from the 15×13 pixel image sent to the network of monadic AMLEs. After each training iteration with a model image, the network’s ability to distinguish the appearance of a cat improves. The feature subtleties can then be captured from the model representation, giving us a valuable means to distinguish a cat from other objects. To test the model representation, we use the testing images shown in Fig. 5e to compare them with the representation of the cat  $r$  and measure the error function with respect to the reference  $i$ , given by  $\tanh((r_j - im_j)^2 e)$  for every pixel  $j$ . Our results, summarized in Fig. 5f, reveal that *Testing Image 1, 3 and 5* resemble the model representation in Fig. 5d. With the error of Image 2, 4, 6 above the threshold (squared Euclidean distance  $\sum (r_j - im_j)^2 = 20$ ), the network predicts that these images are not of a cat. The associative learning network thus accurately classifies images of cats from the model representation obtained from the training iterations.

### **Other evaluation metrics for associative learning devices**

The pattern and image recognition tasks (and in general any form of data transformation) introduced in prior sections can be computed entirely via software simulations running on generic CPUs alone. However, given the large data load that machine learning tasks

typically require, it is essential to reduce the computational effort by offloading or replacing software simulations with dedicated hardware acceleration systems, for instance the purpose-built associative learning network discussed in our work. Although our application-specific system offers greater computational performance from a hardware architectural standpoint, there are still open questions on how the AMLE (which forms the network system) fares relative to its other-platform equivalent on a device-level.

**Table 1.** Comparison of active volume and learning energy in associative learning devices

Type	Active volume ( $\mu\text{m}^3$ )	Min. learning energy (nJ)	Ref.
<b>Electronic</b>			
▪ Memresistive			
i. Chalcogenide	0.12 – 10.5	$4.7 \times 10^4$	(17)
	8	2.63	(18)
ii. Manganite	$\sim 0.1$	$1.35 \times 10^3$	(19)
	$1.25 \times 10^{10}$	$1.02 \times 10^5$	(20)
iv. Nickelate	$4.7 \times 10^3$	$7.20 \times 10^5$	(21)
	$4.8 \times 10^4$	$2.04 \times 10^5$	(22)
v. Metal oxide	900	$4.5 \times 10^3$	(23)
vi. Organic	$\sim 0.5$	$9.75 \times 10^3$	(24)
▪ Electrochemical	$6 \times 10^3$	$6 \times 10^4$	(25)
	$9.6 \times 10^5$	125	(26)
▪ Memcapacitive	26.9	$\sim 30$	(27)
<b>Optoelectronic</b>	$1.62 \times 10^3$	$2.1 \times 10^3$	(28)
<b>Optical</b>	0.12	1.8	(this work)

We identify the relevant device-level evaluation metrics by contextualizing the AMLE with a typical machine learning data load, which requires data to be transferred back and forth from the data source to be run using cloud computing and/or supercomputers. For a more energy-efficient locally run neural network, it is important to shrink the network for greater portability and reduce the energy consumption of the learning process. Table 1 summarizes the minimum active volume and learning energy of other associative learning devices (17-28). These electronic and optoelectronic associative learning devices range from  $\sim 0.1$  to  $10^{10} \mu\text{m}^3$  in active volume and consume  $\sim 2.63$  to  $10^5$  nJ of energy per learning event (17-28). In comparison, the all-optical AMLE in our work fares favorably relative to these devices in terms of dimensions and energy usage, with a low active volume at  $0.12 \mu\text{m}^3$  and minimum learning energy at 1.8 nJ. The single-element device is of dimensions  $3 \mu\text{m} \times 17 \mu\text{m}$ .

## Conclusion

Our results show the first demonstration of an associative monadic learning element (AMLE) implemented on a photonic platform; this can pave the way for further realizations of photonic intelligent systems that can infer probabilistically via associations, in an integrated system of AMLEs. We also provide a supervised learning framework that facilitates the transition from a monadic Pavlovian single *Input-Teacher* association on an AMLE to any arbitrary  $n$  *Input-Teacher* associations, thus enabling backpropagation-free, single-layer architectures.

We have elucidated the inner workings of the network building block, that can spatiotemporally correlate two initially distinct inputs (*UCS* and *NS/CS*) to a single input (*UCS*) when both the inputs are simultaneously applied at a predetermined  $\Delta t$  pulse timing. Given that light signals inherently do not interfere at different wavelengths in linear media (including the AMLE), such input-input association can in principle handle associations of multiple data

streams consisting of different wavelengths over a single element, as we have experimentally demonstrated. Our photonic platform allows for wavelength-multiplexing, which is inherently suited to the highly parallel nature of machine learning. We anticipate further improvements in other relevant metrics (e.g., active volume and learning energy) on different materials platform and with other optimization methods.

On a more general perspective, the two cascaded configuration scheme demonstrated here can extend the typical one-way learning ( $NS/CS$  becomes associated to  $UCS$ ;  $NS/CS \rightarrow UCS$ ) to a customizable form of learning, for example the mutual two-way learning ( $NS/CS \rightleftharpoons UCS/NCS$  where  $NCS$  is the neutral conditioned stimulus). This customizable feature when combined with demonstrations of deterministic weights using identical, fixed energy and fixed-duration pulses (38), will provide unprecedented design flexibility for a wide range of machine learning applications. The compact single-element implementation in our work will allow use of the AMLE as a building block in machine learning/statistical inference in general, thus potentially opening up new avenues of research in machine learning architectures and algorithms.

## METHODS

### Signatures of associative learning

A simple yet intuitive relation between the output response  $R$  and input stimuli  $S$  of the AMLE can be expressed in the compact matrix notation  $R = M_{(II)}M_{(I)}S$ , where the  $2 \times 1$  column vector  $S = (UCS \ NS/CS)^T$ , while the  $2 \times 2$  and  $1 \times 2$  matrices that describe the first and second segments of AMLE are given by:

$$M_{(I)} = \begin{pmatrix} \cos(\kappa l_1) & i \sin(\kappa l_1) \\ i \sin(\kappa l_1) & \cos(\kappa l_1) \end{pmatrix}, \text{ before learning} \quad (1)$$

$$M_{(II)} = \begin{cases} \frac{e^{-\kappa l_2 \cosh \theta_b}}{\sinh \theta_b} (\sinh(\kappa l_2 \sinh \theta_b + \theta_b) & i \sinh(\kappa l_2 \sinh \theta_b)) \\ \frac{e^{-\kappa l_2 \sin \theta_a}}{\cos \theta_a} (\cos(\kappa l_2 \cos \theta_a - \theta_a) & i \sin(\kappa l_2 \cos \theta_a)) \end{cases}, \text{ after learning} \quad (2)$$

in which  $\kappa$  is the waveguide mode coupling coefficient,  $l_1$  and  $l_2$  are the lengths of the first and second segments,  $\theta_b = \cosh^{-1}(\gamma_{crys}/4\kappa)$  and  $\theta_a = \sin^{-1}(\gamma_{aml}/4\kappa)$ .

In the first segment, when two identical inputs  $E_0$  of the same wavelength  $\lambda_0$  are sent to the AMLE, the total field coupled to the respective waveguides is the product of matrix  $M_{(I)}$  and column vector  $(e^{-i\omega\Delta t} \ 1)^T$ , where  $\omega = (2\pi c/\lambda_{eff})$ ,  $c$  is the vacuum speed of light,  $\lambda_{eff} = \lambda_0/n_{eff}$  is the effective wavelength, and  $n_{eff}$  is the effective refractive index. It follows that the field intensity at the lower waveguide is  $|E_{l_1}|^2_{two} = E_0^2 (1 + \sin(2\kappa l_1) \sin(\omega\Delta t))$ . In comparison, when only one input is sent to the AMLE, the coupled field intensity is  $|E_{l_1}|^2_{one} = E_0^2 \sin^2(\kappa l_1)$ . Thus, the critical coupling (maximum energy transfer) length is  $l_{crit} = \pi/\kappa$  for single-input incidence and  $l_{crit}/2$  (at  $\omega\Delta t = \pi/2$ ) for two-input incidence. Given  $\kappa = 0.157 \mu\text{m}^{-1}$  in our case, we have  $|E_{l_1}|^2_{two} = 1.588$  (for  $\omega\Delta t = \pi/2$ ) and  $|E_{l_1}|^2_{one} = 0.095$  at  $l_1 = 2 \mu\text{m}$ . From PCM switching energy threshold perspective, the ratio  $|E_{l_1}|^2_{two}/(1-|E_{l_1}|^2_{one}) = 1.755$  is indicative of associative learning because of the significant energy surplus upon two-input incidence relative to the maximum energy from one-input incidence.

In the second cascade, the relative change in output response  $R$ , which we measure for single-input incidences, can be estimated largely based on  $M_{(II)}$  because  $|E_{l_1}|^2_{one}$  in the first cascade ( $l_1 = 2 \mu\text{m}$ ) is negligibly low. Thus, the ratio  $\eta = |R_{NS/CS}/R_{UCS}|^2$  can be approximated as  $\eta \approx |M_{(II)12} / M_{(II)11}|^2$ . This leads to  $\eta_b \approx |\sinh(\kappa l_2 \sinh \theta_b) / \sinh(\kappa l_2 \sinh \theta_b + \theta_b)|^2$  and  $\eta_a \approx |\sin(\kappa l_2 \cos \theta_a) / \cos(\kappa l_2 \cos \theta_a - \theta_a)|^2$  (subscript 'b' and 'a' denote before and after learning). We additionally denote the output transmission difference between  $UCR_b$  and  $UCR_a$  as  $\Delta|R|^2 = |M_{(II)11b}|^2 - |M_{(II)11a}|^2$  where the alphabetic subscripts likewise denote the learning states. Given

$\gamma_{crys} = 7.65\kappa$  and  $\gamma_{am} = 0.24\kappa$  in our case,  $\eta_b \approx 0.072$  and  $\eta_a \approx 1.006$  at  $l_2 = 15 \mu\text{m}$ . We readily attain  $\eta_b \ll \eta_a$  due to the unbounded  $\sinh$  and positive unbounded  $\cosh$  functions which cause  $\eta_b \rightarrow 0$  with the substantially large  $\gamma_{crys}$ . The set of relations  $\eta_b \ll \eta_a$  and  $\eta_a \approx 1$  is the second signature of associative learning because the output  $R$  upon  $NS/CS$  input incidence transitions from a significantly low value ( $\eta_b \ll \eta_a$ ) to that of  $UCS$  ( $\eta_a \approx 1$ ) which remains within the same transmission range ( $\Delta|R|^2 < 0.5$ ).

### **FDTD simulation**

Three dimensional finite difference time domain (FDTD) simulations are performed using the FDTD Solutions software from Lumerical Inc. A fundamental quasi-transverse electric (TE; magnetic field component  $H_z$  dominant) optical mode source input of 1 V/m at 1580 nm wavelength is let incident onto the AMLE waveguide input. The results shown in the text are the amplitudes of the electric field at the central cross section in the  $x$ - $y$  plane and  $y$ - $z$  plane of the structure for the main plots.

### **Device fabrication and characterization**

The AMLE is fabricated on a  $\text{Si}_3\text{N}_4/\text{SiO}_2$  platform. Electron beam lithography (JEOL 5500FS, JEOL Ltd.) is used at 50kV to define the  $\text{Si}_3\text{N}_4$  structure on the Ma-N 2403 negative-tone resist-coated substrate. After the development process, reactive ion etching (PlasmaPro 80, Oxford Instruments) is performed in  $\text{CHF}_3/\text{O}_2/\text{Ar}$  to etch down 330 nm of  $\text{Si}_3\text{N}_4$ . Electron beam lithography is then implemented on a poly(methyl methacrylate) (PMMA) positive resist-coated substrate to open a window for the PCM cell. This is followed by sputter-deposition of 10-nm GST/10-nm ITO on the substrate. The AMLE characterization process is performed using high resolution emission gun SEM (Hitachi S-4300 SEM system- Ibaraki, Japan) with low accelerating voltage (1 to 3kV) at working distance of  $\sim 13\text{mm}$ .

### **Optical measurement**

The AMLE optical measurement setup (for Fig. 2) builds upon previously described probe-pump configuration (34). Two low-power continuous-wave (CW) probe diode lasers (N7711A, Keysight Technologies) are used as probe lasers to measure the transmission through AMLE. To measure the probe signals after transmission through AMLE, the signals are filtered by optical tunable band-pass filters (OTF-320, Santec Corp.) and detected by photodetectors (2011-FC, Newport Spectra-Physics Ltd.). The pump pulse is generated from a CW diode laser (TSL-550, Santec Corp.) modulated by the electro-optic modulator (EOM) (2623NA, Lucent) which is controlled by an electrical arbitrary pulse generator (AFG 3102C, Tektronix), to be amplified by a low-noise erbium-doped fiber amplifier (AEDFA-CL-23, Amonics).

In the stabilization step carried out prior to the experiment, a set of amorphizing pulses are sent to the AMLE, followed by a set of crystallizing pulses. These sets of pulses are exactly the same as the pulses applied during the ‘associative learning’ and ‘forgetting’ process shown in Fig. 3a. Here, the set of amorphizing pulses is the consecutive 100 ns-wide pulses at 6.6 mW, 8.7 mW, 12.6 mW and 14.5 mW, while the set of crystallizing pulses is the 100 ns-wide pulse at 4.3 mW for ten times, followed by five 1.9 mW 100 ns-wide pulses at 1 MHz repetition rate for ten times.

In our measurement setup for supervised learning (using thermo-optic heaters), inputs  $IN_1$  and  $IN_2$  are mapped to the possible input combinations, and represented as optical field emitted from the respective CW lasers (N7711A, Keysight Technologies) coupled to single-mode fibers. A separate supervisory *Teacher* signal is distributed to each of the ( $IN_1, IN_2$ ) signal combinations. The combined signals are channeled to a pair of optical switches each, which selectively route the signals to either probe or pump line. At the output end of the layout, the readouts are filtered by OTF (OTF-320, Santec Corporation) and detected by photodetector (2011-FC, Newport Spectra-Physics Ltd.). During pumping, the optical attenuator (V1550PA, Thorlabs Inc.) connected prior to the filter is activated to null the signals to the photodetector.



To induce the optical phase shifts, these coupled signals are modulated by NiCr thermo-optic heaters via voltage biasing.

The image recognition results in Fig. 5 is obtained from our experiments. We note that the number of AMLEs in the associative network can be reduced e.g., via self-organizing dimensionality reduction method (30,47).

**Acknowledgements:** The authors acknowledge discussions with Andrew Katumba. Nikolaos Farmakidis, Eugene J. H. Soh and Wen Zhou. J.Y.S.T. thanks Hazim Hanif for stimulating conversations. **Funding:** This research was supported via the Engineering and Physical Sciences Research Council Manufacturing Fellowship EP/J018694/1, the Wearable and Flexible Technologies (WAFT) collaboration (EP/M015173/1), and the Chalcogenide Advanced Manufacturing Partnership (EP/M015130/1). **Author contributions:** H.B., C.D.W., and W.H.P.P. led the project. H.B., J.Y.S.T. and Z.C. conceived, planned the project, and drafted the manuscript. J.Y.S.T. and Z.C. performed the analytical calculations, simulations, fabrications, and characterizations. All authors discussed the results and manuscript.

## References

- 1 Piaget, J. *The origins of intelligence in children* (International Universities Press, 1936).
- 2 Plomin, R., Fulker, D. W., Corley, R. & DeFries, J. C. Nature, nurture and cognitive development from 1 to 16 years: A parent-offspring adoption study. *Psychol. Sci* **8**, 442-447 (1997).
- 3 Nilsson, N. J. *The quest for artificial intelligence* (Cambridge University Press, 2009).
- 4 Turing, A. M. Computing machinery and intelligence *Mind* **49**, 433-460 (1950).
- 5 Schuman, C. D. *et al.* A survey of neuromorphic computing and neural networks in hardware. *arXiv: 1705.06963v06961* (2017).
- 6 Furze, T. A. & Bennett, B. in *Proceedings of the Artificial Intelligence and the Simulation of Behaviour (AISB) Conference 2011*. (eds D. Kazakov & G. Tsoulas) 40-47 (Society for the Study of Artificial Intelligence and the Simulation of Behaviour, York, U.K.).
- 7 Andreae, J. H. *Associative learning for a robot intelligence* (Imperial College Press, 1998).
- 8 Usama, M. *et al.* Unsupervised machine learning for networking: Techniques, applications and research challenges. *arXiv:1709.06599* (2017).

- 9 Velasco, B. A. M., Herranz, Á. G., López, M. Á., Pulvirenti, F. & Maravitsas, N. in *Proceedings of the First International Workshop on Big Data Applications and Principles*. 103-134 (Springer International Publishing).
- 10 Bolton, R. J. & Hand, D. J. Statistical fraud detection: A review. *Stat. Sci.* **17**, 235-255 (2002).
- 11 Koyuncugil, A. S. & OZgulbas, N. *Surveillance technologies and early warning systems: Data mining applications for risk detection*. (Information Science Reference, 2011).
- 12 Paine, T., Jin, H., Yang, J., Lin, Z. & Huang, T. GPU asynchronous stochastic gradient descent to speed up neural network training. *arXiv:1312.6186* (2013).
- 13 Jouppi, N. P. *et al.* in *ISCA '17: Proceedings of the 44th Annual International Symposium on Computer Architecture*.
- 14 Cassidy, A. S., Georgioub, J. & Andreou, A. G. Design of silicon brains in the nano-CMOS era: Spiking neurons, learning synapses and neural architecture optimization. *Neural Netw.* **45**, 4-26 (2013).
- 15 Gschwind, M. *et al.* Synergistic processing in cell's multicore architecture. *IEEE Micro* **26** (2006).
- 16 Misra, J. & Saha, I. Artificial neural networks in hardware: A survey of two decades of progress. *Neurocomputing* **74**, 239-255 (2010).
- 17 Ziegler, M. *et al.* An electronic version of Pavlov's dog. *Adv. Function. Mater* **22**, 2744–2749 (2012).
- 18 Li, Y. *et al.* Associative learning with temporal contiguity in a memristive circuit for large-scale neuromorphic networks. *Adv. Electron. Mater* **1**, 1500125 (2015).
- 19 Moon, K. *et al.* Hardware implementation of associative memory characteristics with analogue-type resistive switching device. *Nanotechnol.* **25**, 495204 (2014).
- 20 Tan, Z.-H. *et al.* Pavlovian conditioning demonstrated with neuromorphic memristive devices. *Sci. Rep.* **7**, 713 (2017).
- 21 Hu, S. G. *et al.* Synaptic long-term potentiation realized in Pavlov's dog model based on a NiOx-based memristor. *J. Appl. Phys.* **116**, 214502 (2014).
- 22 Ha, S. D., Shi, J., Meroz, Y., Mahadevan, L. & Ramanathan, S. Neuromimetic circuits with synaptic devices based on strongly correlated electron systems. *Phys. Rev. App.* **2**, 064003 (2014).
- 23 Wu, C. *et al.* Mimicking classical conditioning based on a single flexible memristor. *Adv. Mat.* **29**, 1602890 (2017).
- 24 Bichler, O. *et al.* Pavlov's dog associative learning demonstrated on synaptic-like organic transistors. *Neural Comput.* **25**, 549-566 (2013).
- 25 Wan, C., Zhou, J., Shi, Y. & Wan, Q. Classical conditioning mimicked in junctionless IZO electric-double-layer thin-film transistors. *IEEE Electron. Dev. Lett.* **35** (2014).
- 26 Yu, F., Zhu, L. Q., Xiao, H., Gao, W. T. & Guo, Y. B. Restickable oxide neuromorphic transistors with spike-timing-dependent plasticity and Pavlovian associative learning activities. *Adv. Funct. Mater* **28**, 1804025 (2018).
- 27 Wang, Z. *et al.* Capacitive neural network with neuro-transistors. *Nat. Commun.* **9**, 3208 (2018).
- 28 John, R. A. *et al.* Synergistic gating of electro-iono-photoactive 2D chalcogenide neuristors: Coexistence of Hebbian and homeostatic synaptic metaplasticity. *Adv. Mat.* **30**, 1800220 (2018).
- 29 Zhang, H. *et al.* Programming a Pavlovian-like conditioning circuit in Escherichia coli. *Nat. Commun.* **5**, 3102 (2014).

- 30 Alkon, D. L., Blackwell, K. T., Barbour, G. S., Rigler, A. K. & Vogl, T. P. Pattern-  
recognition by an artificial network derived from biologic neuronal systems. *Biol.*  
*Cybern* **62**, 363-376 (1990).
- 31 Lederhendler, I. I., Gart, S. & Alkon, D. Classical conditioning of Hermissenda: Origin  
of a new response. *J. Neurosci.* **6**, 1325-1331 (1986).
- 32 Commins, S. in *Behavioral neuroscience* Ch. 9, 100-117 (Cambridge University Press,  
2018).
- 33 Pavlov, I. P. Conditioned reflexes: An investigation of the physiological activity of the  
cerebral cortex. *Ann. Neurosci.* **17**, 136–141 (1927).
- 34 Ríos, C. *et al.* Integrated all-photonics non-volatile multi-level memory. *Nat. Photon.* **9**,  
725-733 (2015).
- 35 Siegel, J., Schropp, A., Solis, J., Afonso, C. N. & Wuttig, M. Rewritable phase-change  
optical recording in Ge<sub>2</sub>Sb<sub>2</sub>Te<sub>5</sub> films induced by picosecond laser pulses. *Appl. Phys.*  
*Lett.* **84**, 2250 (2004).
- 36 Xie, Y. *et al.* Self-healing of a confined phase change memory device with a metallic  
surfactant layer. *Advanced Materials* **30**, 1705587 (2018).
- 37 Pirovano, A. *et al.* in *IEEE International Electron Devices Meeting.* 699-702 (Institute  
of Electrical and Electronics Engineers (IEEE)).
- 38 Cheng, Z., Ríos, C., Pernice, W. H. P., Wright, C. D. & Bhaskaran, H. On-chip photonic  
synapse. *Sci. Adv.* **3** (2017).
- 39 Haus, H. A. & Huang, W. Coupled-mode theory. *Proc. IEEE* **79**, 1505-1518 (1991).
- 40 Wolpert, D. H. *The supervised learning no free-lunch theorems.* (Springer, 2001).
- 41 Wolpert, D. H. The lack of a priori distinctions between learning algorithms. *Neural*  
*Computation* **8**, 1341-1390 (1996).
- 42 Retrieved from <http://fast.ai/datadogscats.zip/>. Accessed on 10 July 2020.
- 43 Krizhevsky, A. Learning Multiple Layers of Features from Tiny Images. (2009).
- 44 Li Fei-Fei, R. F., Pietro Perona. in *2004 Conference on Computer Vision and Pattern*  
*Recognition Workshop* (IEEE).
- 45 Omkar M Parkhi, A. V., Andrew Zisserman, C. V. Jawahar. in *IEEE Conference on*  
*Computer Vision and Pattern Recognition* (IEEE).
- 46 Jia Deng, W. D., Richard Socher, Li-Jia Li, Kai Li, Li Fei-Fei. in *2009 IEEE Conference*  
*on Computer Vision and Pattern Recognition* (IEEE).
- 47 Barbour, G., Blackwell, K., Busse, T., Alkon, D. & Vogl, T. Dystal: a Self-organizing  
ANN with Pattern Independent Training Time *Intern. Join. Conf. Neur. Net.* **4**, 814-  
819 (1992).